The GASS/EUCLIPSE model intercomparison of the stratocumulus transition as observed during ASTEX: LES results

J. J. van der Dussen,[1] S. R. de Roode,[1] A. S. Ackerman,[2] P. N. Blossey,[3] C. S. Bretherton,[3] M. J. Kurowski,[4,5] A. P. Lock,[6] R. A. J. Neggers,[7,8] I. Sandu,[9,10] and A. P. Siebesma[1,11]

[1] Large-eddy simulations of a Lagrangian transition from a vertically well-mixed stratocumulus-topped boundary layer to a situation in which shallow cumuli penetrate an overlying layer of thin and broken stratocumulus are compared with aircraft observations collected during the Atlantic Stratocumulus Transition Experiment. Despite the complexity of the case and the long simulation period of 40 h, the six participating state-of-the-art models skillfully and consistently represent the observed gradual deepening of the boundary layer, a negative buoyancy flux at the top of the subcloud layer and the development of a double-peaked vertical velocity variance profile. The moisture flux from the subcloud to the stratocumulus cloud layer by cumulus convection exhibits a distinct diurnal cycle. During the night the moisture flux at the stratocumulus cloud base exceeds the surface evaporation flux, causing a net drying of the subcloud layer, and vice versa during daytime. The spread in the liquid water path (LWP) among the models is rather large during the first 12 h. From additional sensitivity experiments it is demonstrated that this spread is mainly attributable to differences in the parameterized precipitation rate. The LWP differences are limited through a feedback mechanism in which enhanced drizzle fluxes result in lower entrainment rates and subsequently a reduced drying at cloud top. The spread is furthermore reduced during the day as cloud layers with a greater LWP absorb more solar radiation and hence evaporate more.

Citation: van der Dussen, J. J., S. R. de Roode, A. S. Ackerman, P. N. Blossey, C. S. Bretherton, M. J. Kurowski, A. P. Lock, R. A. J. Neggers, I. Sandu, and A. P. Siebesma (2013), The GASS/EUCLIPSE model intercomparison of the stratocumulus transition as observed during ASTEX: LES results, *J. Adv. Model. Earth Syst.*, *5*, 483–499, doi:10.1002/jame.20033.

[1]Department of Geoscience and Remote Sensing, Delft University of Technology, Delft, Netherlands.

[2]NASA Goddard Institute for Space Studies, New York, USA.

[3]Department of Atmospheric Sciences, University of Washington, Seattle, USA.

[4]Institute of Geophysics, Faculty of Physics, University of Warsaw, Warsaw, Poland.

[5]Institute of Meteorology and Water Management-National Research Institute, Warsaw, Poland.

[6]Foundation Science, Met Office, Exeter, UK.

[7]Department of Regional Climate, Royal Netherlands Meteorological Institute, De Bilt, Netherlands.

[8]Institut für Geophysik und Meteorologie, Universität zu Köln, Köln, Germany.

[9]Department of Atmosphere in the Earth System, Max-Planck Institut für Meteorologie, Hamburg, Germany.

[10]Section of Physical Aspects, European Centre for Medium-Range Weather Forecasts, Reading, UK.

[11]Atmospheric Research Division, Royal Netherlands Meteorological Institute, De Bilt, Netherlands.

1. Introduction

[2] Large portions of the Earth's oceans are covered by fields of stratocumulus clouds [*Wood*, 2012]. As these clouds are advected from the subtropics toward the equator by the trade winds, they are gradually replaced by shallow cumulus clouds. Because these cumuli have a much lower area coverage, the radiative forcing of the two cloud types is very different. Stratocumulus to cumulus transitions are therefore key to the subtropical energy balance, making it crucial for numerical weather prediction and global climate models to accurately capture them. However, *Teixeira et al.* [2011] showed that these transitions often occur too early as compared with observations, which partly causes the underestimation of the subtropical low cloud amount many such models suffer from.

[3] The first numerical studies on stratocumulus cloud transitions were performed with one- or two-dimensional turbulence models [e.g., *Krueger et al.*, 1995;

Bretherton and Wyant, 1997; *Wyant et al.*, 1997; *Bretherton et al.*, 1999; *Svensson et al.*, 2000]. Owing to the continuous advance in the amount of available computational power, three-dimensional large-eddy simulation (LES) modeling on a sufficiently large domain and for sufficiently long time periods has now become feasible as is demonstrated by *Sandu and Stevens* [2011]. Their results show that LES models are well capable of representing a smooth transition between the two cloud regimes. However, because the cases were based on composites of satellite observations and reanalysis data [*Sandu et al.*, 2010], features like the evolution of the mean state and turbulence structure of the boundary layer could not be critically compared with in situ observations.

[4] Another approach to determine what processes cause the stratocumulus to cumulus transition is to perform idealized simulations toward an equilibrium state [*Zhang et al.*, 2010]. Using this methodology, *Chung et al.* [2012] found that the steady-state inversion height increases as the sea surface temperature (SST) is increased. The boundary layer structure furthermore changes from relatively well mixed to decoupled with cumulus clouds developing underneath a thin stratocumulus layer. The stratocumulus cloud layer eventually vanishes at sufficiently high SSTs. On the basis of Lagrangian LES experiments, *Sandu and Stevens* [2011] also concluded that the SST is the main factor explaining the stratocumulus transition. *Klein and Hartmann* [1993] furthermore showed that the seasonally averaged cloud fraction typically increases with lower tropospheric stability, which is a measure of vertical stability and is defined as the potential temperature difference between the 700 hPa level and the surface.

[5] During the first Lagrangian of the Atlantic Stratocumulus Transition Experiment (ASTEX), aircraft observations of a transition from a solid stratocumulus-topped boundary layer to a boundary layer dominated by shallow cumulus clouds penetrating a thin veil of broken stratocumulus were collected [*Albrecht et al.*, 1995; *Bretherton and Pincus*, 1995; *Bretherton et al.*, 1995; *De Roode and Duynkerke*, 1997]. These observations were used by *Bretherton et al.* [1999] to set up a model intercomparison case in order to study the representation of the entire transition with single-column model (SCM) versions of numerical weather prediction and climate models as well as with two-dimensional turbulence models. All models were shown to be able to predict the deepening and decoupling of the boundary layer and the appearance of cumuli below the stratocumulus clouds. However, significant quantitative differences were found in the liquid water path (LWP) and cloud cover that were ascribed to the parameterizations of radiation, microphysics and subgrid-scale turbulence.

[6] Two model intercomparison studies for both SCM and LES models were set up on the basis of the second (A209) and the third flight (RF06) [*Duynkerke et al.*, 1999; *Chlond and Wolkau*, 2000] of the ASTEX first Lagrangian as part of the Global Energy and Water Cycle Experiment (GEWEX) Cloud System Study (GCSS) project. Due to the limited computa-

Table 1. Values of the Parameters Used in Equation (1) to Describe the Initial Profiles of the Relevant Variables

φ	φ_{ml}	$\Delta\varphi$	Γ_φ (km^{-1})
q_T (g kg^{-1})	10.2	−1.1	2.8
θ_L (K)	288.0	5.5	−6.0
u (m s^{-1})	−0.7	−1.3	0.0
v (m s^{-1})	−10.0	0.0	0.0

tional resources, the LES runs lasted just 3 h and used a rather coarse vertical grid resolution. The results suggested that the entrainment rate in the LES models was on average about 50% greater than the values derived from the aircraft observations. However, the entrainment rate was shown to decrease if cloud microphysics was included or if the vertical resolution was increased.

[7] In this paper, some slight modifications to the ASTEX first Lagrangian model intercomparison case proposed by *Bretherton et al.* [1999] are described and the simulation results of six state-of-the-art LES models are presented. These models each include detailed parameterization schemes for radiation and microphysics. The aim is to assess how well LES models are capable of representing stratocumulus transitions by making a detailed comparison with the observations. Together with the three stratocumulus transition cases designed by *Sandu and Stevens* [2011], this case was run as a joint Global Atmospheric System Study (GASS) and European Union Cloud Intercomparison, Process Study and Evaluation (EUCLIPSE) project effort. *De Roode et al.* [2012] presents the preliminary LES results of all four cases and discusses the development of stratocumulus transitions under different forcing conditions. The simulation results of the SCM versions of numerical weather prediction and climate models will be presented and compared with the LES results in a separate paper.

[8] The setup of the paper is as follows. Section 3 describes the initialization of the case, the boundary conditions and the large-scale forcings as well as numerical aspects such as resolution and domain size. The results submitted by the participating modelers are compared with the observations in section 3. In section 4, the humidity budget is analyzed with particular attention to drizzle and surface latent heat fluxes. The last section contains a summary of the main conclusions and some discussion.

2. Setup

2.1. Initial Conditions

[9] The initial vertical profiles are taken from the GCSS model intercomparison case based on flight 2 of the ASTEX first Lagrangian, which was set up by Peter Duynkerke. These profiles are given by

$$\varphi(z) = \begin{cases} \varphi_{ml} & z \leq z_i \\ \varphi_{ml} + \Delta\varphi(z-z_i)/\Delta z & z_i < z \leq z_i + \Delta z \\ \varphi_{ml} + \Delta\varphi - \\ \Gamma_\varphi(z-z_i-\Delta z) & z_i + \Delta z < z \leq 2\,\text{km} \end{cases} \quad (1)$$

where $\varphi \in \{q_T, \theta_L, u, v\}$ are the total specific humidity, the liquid water potential temperature and the wind
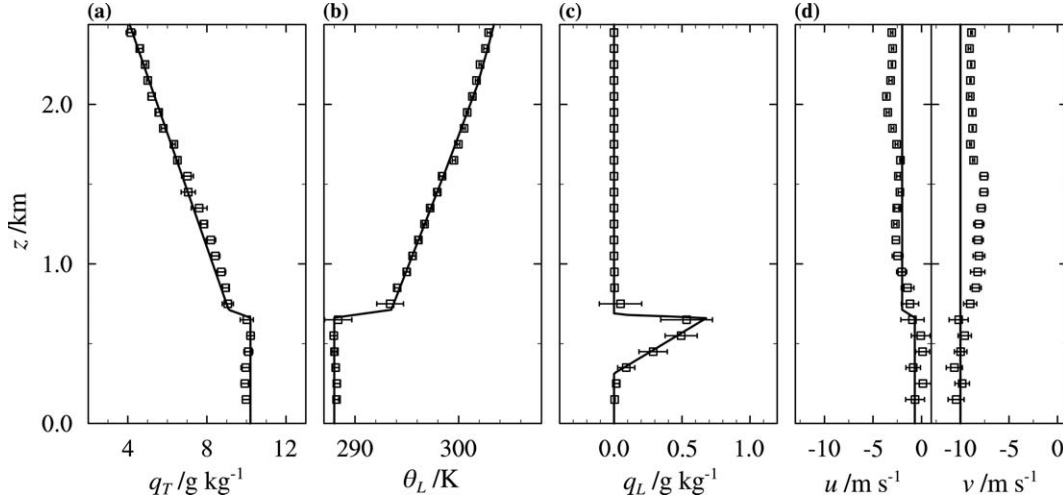
Figure 1. Initial profiles of (a) total humidity q_T, (b) liquid water potential temperature θ_L, (c) liquid water specific humidity q_L, and (d) horizontal wind components u (east-west) and v (south-north). Squares denote observations gathered during flight 2 of the first Lagrangian, bin averaged over height intervals of 100 m. Error bars show the ± 1 standard deviation range.

components in east-west and south-north directions, respectively. Initial values of the mixed layer variables φ_{ml}, the inversion jumps $\Delta\varphi$ and the free atmospheric lapse rates Γ_φ for each of these variables are given in Table 1. The inversion layer initially has a thickness of $\Delta z = 50$ m and its base is at a height $z_i = 662.5$ m. The initial profile for the pressure is constructed by assuming hydrostatic equilibrium, with a surface pressure $p_s = 1029.0$ hPa that is constant in time. The motivation for choosing the second flight of the ASTEX first Lagrangian is that the boundary layer was vertically well mixed and horizontally homogeneous, making it a more suitable starting point than the first flight during which the boundary layer structure was inhomogeneous with occasional small cumuli and fog [*De Roode and Duynkerke*, 1997]. The simulations start 13 June 1992 at 0000 universal coordinated time (UTC) and last 40 h, approximately corresponding to the time between ASTEX measurement flights 2 and 5.

[10] The initial vertical profiles defined by equation (1) are shown in Figure 1 together with the observations from which the profiles were originally derived. Above 2 km, the profiles are determined from ECMWF reanalysis (ERA)-Interim reanalysis data as described in section 2.2.4. Note that all the necessary model input data presented in this section can be downloaded from the EUCLIPSE project website (www.euclipse.nl/wp3/ASTEX_Lagrangian/LES_astex_setup.shtml).

2.2. Model Forcings

[11] The ASTEX observations were performed following a Lagrangian strategy during which a column of air was followed as it was advected toward the equator. An advantage of this approach is that the effect of horizontal advection on the budgets of heat and moisture can be neglected, provided that the vertical shear of horizontal winds is negligibly small. Time-varying forcings and boundary conditions are prescribed to account

for changing conditions along the Lagrangian trajectory. They differ slightly from the forcing prescribed by *Bretherton et al.* [1999]. For example, a relaxation toward the observed mean winds is not required in the current setup.

2.2.1. Sea Surface Temperature

[12] The SST time series as compiled by *Bretherton et al.*, [1995, Figure 1a] is used for the simulations, which contains reanalysis data supplied by the European Centre for Medium-Range Weather Forecasts (ECMWF) and measurements from two aircraft and a ship. These data give a relatively fast SST increase of about 4 K over the 40 h simulation period. In contrast to the GCSS model intercomparison cases based on flights 2 and 3 that used prescribed surface fluxes, the surface fluxes are here computed from the prescribed SST.

2.2.2. Geostrophic Wind

[13] Figure 2a shows that the mean wind velocity in both the boundary layer and the free atmosphere changed from a mainly north to a north-east direction during the transition. We estimated the temporal variation of the geostrophic wind velocity using the observed wind components in the free atmosphere and their respective budget equations,

$$\frac{\partial u_{fa}}{\partial t} = f\left(v_{fa} - v_g\right), \qquad (2a)$$

$$\frac{\partial v_{fa}}{\partial t} = -f\left(u_{fa} - u_g\right). \qquad (2b)$$

[14] Here the subscript "fa" indicates free atmospheric values, f is the Coriolis parameter and u_g and v_g are the horizontal components of the geostrophic wind. Figure 2a shows the estimated geostrophic wind components, which are assumed to be constant with height. It can
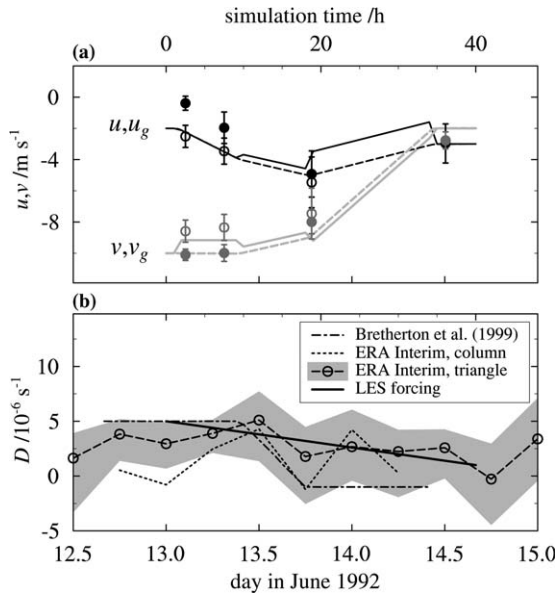
Figure 2. (a) The geostrophic wind (solid lines) and the expected free atmospheric horizontal wind components calculated using equation (2) (dashed) as a function of time. The filled and the open circles, respectively, indicate the observed boundary layer and free atmospheric velocities. (b) The boundary layer averaged large-scale divergence of the horizontal winds D as derived from ERA-40 data by *Bretherton et al.* [1999] (dash-dotted). The dotted line was obtained by taking a weighted area and a boundary layer average of D from ERA-Interim data along the trajectory as reported by *Bretherton and Pincus* [1995]. The dashed line represents the boundary layer averaged D, averaged over the ASTEX triangle [*Albrecht et al.*, 1995]. The area between the 20th and the 80th percentile has been shaded in gray. The large-scale divergence that was used for the simulations is indicated by the solid black line.

also be noticed from this figure that the horizontal winds in the free atmosphere will be correctly predicted if this prescribed geostrophic forcing is used in a time integration of equation (2). The prescribed geostrophic forcing will furthermore enforce a weakening of the total horizontal boundary layer wind speed, which was observed to decrease from 10 to approximately 4 m s^{-1} during the Lagrangian. Note that Figure 2a also indicates that the observed wind shear across the inversion is generally less than 2 m s^{-1}, suggesting that the influence of horizontal advection of q_T and θ_L into the Lagrangian column is small. The variation of the horizontal wind with time needs to be accounted for in the model simulations as it controls the magnitude of the surface fluxes of momentum, heat and moisture. These surface fluxes were all calculated using a fixed surface roughness length $z_0 = 2 \times 10^{-4}$ m.

2.2.3. Large-Scale Divergence

[15] The GCSS model intercomparison cases based on flights 2 and 3 prescribed a large-scale divergence rate D of 5×10^{-6} s^{-1} and 15×10^{-6} s^{-1}, respectively. These values were chosen on the basis of an assumed balance between the large-scale subsidence and the entrainment rate in order to yield an approximate steady-state boundary layer height in the LESs. These prescribed values for D are likely too large because the used LES models were run with a rather coarse vertical resolution and did not include cloud droplet sedimentation, and thus gave unrealistically large entrainment rates. For the ASTEX model intercomparison study by *Bretherton et al.* [1999], a time-varying value for D was applied based on measurements and ECMWF reanalysis data (see Figure 2b). LES runs performed by *De Roode and Van der Dussen* [2010] showed that with these values for D the boundary layer depth is overestimated by almost 1 km as compared to the observations at the end of the 40 h simulation.

[16] *Ciesielski et al.* [1999] used soundings of the horizontal winds to calculate D and the large-scale subsidence for the period 1–15 June 1992. Their results show only a slight and gradual decrease of D during the first Lagrangian, resulting in an average value of about 4×10^{-6} s^{-1}. This finding is in line with the conclusion of *Sigg and Svensson* [2004], who state that there is no evidence for a strong decrease in D as suggested by *Bretherton and Pincus* [1995]. Figure 2b shows D as diagnosed from ERA-Interim data. The spatial and temporal variation in the data is large, as is the case with ERA-40 data [*Duynkerke et al.*, 1999]. The value for D as averaged over the boundary layer column and at the actual position during the Lagrangian therefore fluctuates between about 5×10^{-6} and -1×10^{-6} s^{-1}. *Ciesielski et al.* [2001] found a diurnal signal in D with an amplitude of up to 2×10^{-6} s^{-1} and a similar diurnal cycle was proposed in other studies [e.g., *Bretherton et al.*, 2004]. Due to the low temporal resolution a diurnal cycle cannot be discerned in the ERA-Interim data. When D is averaged over the ASTEX triangle the signal fluctuates less and decreases slightly during the period of the first Lagrangian. On the basis of these studies a simple function for D is prescribed that decreases linearly with time from a value of 5×10^{-6} s^{-1} to 1×10^{-6} s^{-1}. Following *Bretherton et al.* [1999], $D = 0$ above 1600 m such that the subsidence is constant above this height. This forcing produces q_T and θ_L tendencies in the free atmosphere that are close to those observed.

2.2.4. Radiation

[17] Radiative transfer codes are used to provide accurate temperature tendencies due to longwave and shortwave radiation in the LES domain. The background profiles of humidity, temperature and ozone needed in these schemes were obtained from ERA-Interim reanalysis data. These profiles are kept constant in time. The precise amount of cirrus clouds that was present at the end of the Lagrangian [*Ciesielski et al.*, 1999] cannot be quantified from the field observations and is therefore neglected for simplicity.

[18] An important factor for the calculation of both radiative and microphysical effects on the cloud layer is the size of the cloud droplets. The cloud droplet number density N_c is assumed to be constant at 100 cm^{-3}

Table 2. List of the Participating Modelers and the Used Models Including Parameterization Schemes

Modeler	Model	Model Description	Microphysics	Radiation	Advection
A. Ackerman	DHARMA	*Stevens et al.* [2002]	*Morrison et al.* [2005]	*Toon et al.* [1989]	*Stevens and Bretherton* [1996]
P. Blossey	SAM 6.8.2	*Khairoutdinov and Randall* [2003]	*Khairoutdinov and Kogan* [2000]	*Mlawer et al.* [1997], RRTMG	*Smolarkiewicz and Grabowski* [1990]
M. Kurowski	EULAG	*Prusa et al.* [2008]	*Khairoutdinov and Kogan* [2000], single moment	*Briegleb* [1992]	*Smolarkiewicz* [2006]
A. Lock	MOLEM	*Shutts and Gray* [1994]; *Abel and Shipway* [2007]	*Abel and Shipway* [2007]	*Edwards and Slingo* [1996]	*Yamaguchi et al.* [2011]
I. Sandu	UCLA LES	*Stevens and Seifert* [2008]	*Seifert and Beheng* [2001]	*Fu and Liou* [1993]; *Pincus and Stevens* [2009]	*Stevens et al.* [2005]
J. van der Dussen	DALES 3.2	*Heus et al.* [2010]	*Khairoutdinov and Kogan* [2000]	*Fu and Liou* [1993]; *Pincus and Stevens* [2009]	*Blossey and Durran* [2008]

[*Bretherton et al.*, 1995] wherever liquid water is present. A lognormal cloud droplet size distribution is assumed, resulting in a correction factor for the calculation of the effective radius r_e that is a function of the geometric standard deviation σ_g. Using $\sigma_g = 1.2$,

$$r_e = r_V \exp\left[\ln\left(\sigma_g\right)^2\right] \approx 1.03\, r_V, \qquad (3)$$

in which r_V is the mean volume radius of the droplets,

$$r_V = \left(\frac{3\rho_a q_L}{4\pi \rho_L N_c}\right)^{1/3}. \qquad (4)$$

[19] Here ρ_a and ρ_L are the densities of respectively moist air and liquid water and q_L is the liquid water specific humidity. The value of 1.03 in equation (3) is in good agreement with observational findings by *Pawlowska and Brenguier* [2000].

[20] The sea surface albedo α_s is a function of μ, the cosine of the solar zenith angle, and is approximated by [*Briegleb*, 1992]:

$$\alpha_s = \frac{0.026}{\mu^{1.7} + 0.065} + 0.15(\mu - 0.10)(\mu - 0.50)(\mu - 1.00). \qquad (5)$$

2.3. Numerical and Model Details

[21] References to the descriptions of the six participating LES models can be found in Table 2. Following *Sandu and Stevens* [2011], the LES runs were performed using a horizontal domain size of 4480^2 m^2 consisting of 128 grid points with a resolution of 35 m in each horizontal direction. In the *z*-direction a varying vertical grid resolution was used, ranging from 15 m at the surface to 5 m in the cloud layer and at the inversion. The base of the sponge layer is located at approximately 2400 m and above this height the vertical grid distance is stretched with increments of 10% per level. Although it is recognized that the horizontal domain size is rather small, *Sandu and Stevens* [2011] showed that for simulations of

cases with little precipitation a larger horizontal domain size of 8960^2 m^2 hardly affected the LES results.

[22] The domain is translated with a constant velocity of -2 ms^{-1} in the *x*- and -7 ms^{-1} in the *y*-direction. These velocities are chosen as optimal values for computational efficiency.

[23] All modelers were asked to provide the same output data as in the Rain in Cumulus over the Ocean (RICO) model intercomparison [*vanZanten et al.*, 2011].
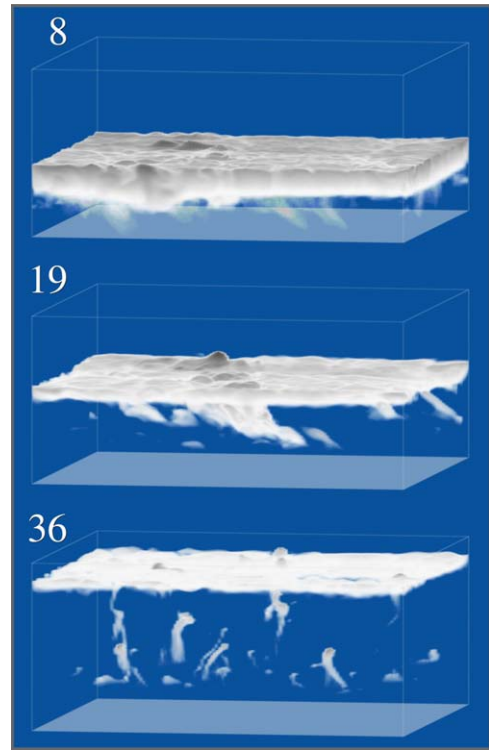

Figure 3. Snapshots of the condensed water (including rain) at 8, 19, and 36 h as simulated using DALES. High q_L values have a darker shade. The white plane indicates the surface. The total height of the box is 2 km.
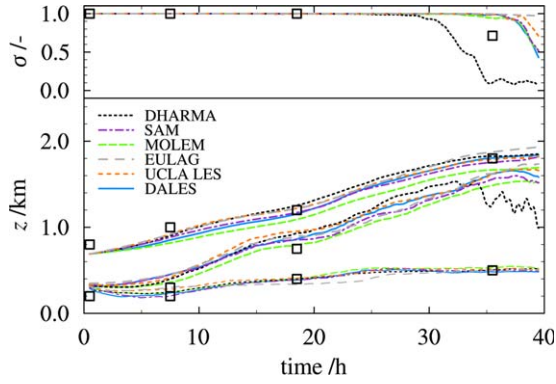
Figure 4. (top) The total cloud cover and (bottom) the contours of the simulated clouds composed of the inversion height z_i as an indication of the mean stratocumulus cloud top, minimum cloud base height $z_{b,\min}$ and mean cloud base height z_b for each of the models shown in the legend. The squares denote similar quantities estimated from the profiles of q_L shown in Figure 7.

3. Model Results and Observations

3.1. Time series

[24] The three snapshots of the cloud fields as obtained from the Dutch Atmospheric LES (DALES) model presented in Figure 3 show the clear evolution during the stratocumulus transition. As the boundary layer gradually deepens, shallow cumulus clouds develop which penetrate the stratocumulus cloud layer above. The onset of the breakup of the thinning stratocumulus is marked by the appearance of clear air patches at the top of the cloud layer.

[25] The domain averaged cloud cover σ presented in Figure 4 (top) shows that only at the end of the simulation does the stratocumulus layer start to break up. All models except distributed hydrodynamic aerosol and radiative modeling application (DHARMA) agree well on the timing of breakup. Figure 4 (bottom) shows the development of the cloud boundaries. In particular, the set of upper lines represents the inversion height z_i, which is typically located just above the stratocumulus cloud top. The middle set of lines depict the domain averaged cloud base height z_b. As the cumulus cloud fraction is very small, the value of z_b is dominated by the stratocumulus cloud base height. The lowest set shows the minimum cloud base height $z_{b,\min}$, which represents the lowest cumulus cloud base height. The stratocumulus cloud base height gradually increases with time, whereas the cumulus cloud base is almost constant. The increasing difference between z_b and $z_{b,\min}$ is indicative of the development of a decoupled boundary layer structure, in which cumulus clouds supply the stratocumulus cloud layer with heat and moisture from the subcloud layer. The general picture of the transition is consistent in the models. Differences in the minimum (cumulus) cloud base height are negligible, while the spread in the modeled inversion height and average cloud base height is of the order of 200 m. This is about

20% of the total inversion height increase over the course of the transition.

[26] Figure 5a shows the entrainment rate w_e as a function of time. Estimates made on the basis of observations [*De Roode and Duynkerke*, 1997] are included as a reference. The diurnal cycle is clearly visible in this plot, with significantly more entrainment during the night as compared to the daytime.

[27] Overall, there is better agreement between the simulated entrainment rates than the simulated LWPs, as has been seen in past LES intercomparison studies for stratocumulus clouds [*Stevens et al.*, 2005; *Ackerman et al.*, 2009]. The relatively good agreement in entrainment rate has been explained in the past as a consequence of the heat budget of the boundary layer, which is dominated by radiative cooling, counterbalanced by heat storage needed to keep the layer warming at a rate similar to the SST, and entrainment warming. Since the other two dominant terms are similar between models, and the inversion potential temperature jump is also similar between models, this argument implies the entrainment rate will be similar between models. However, due to differences in transport and subgrid-scale turbulence, different models require stratocumulus cloud layers of different thickness to maintain a given entrainment rate, hence LWP can vary more substantially between models [e.g., *Zhu et al.*, 2005].

[28] One other term that can be important to the heat budget (and hence entrainment rate) is net latent heating due to surface precipitation. It will be argued in section 4.3 that microphysical processes are the major
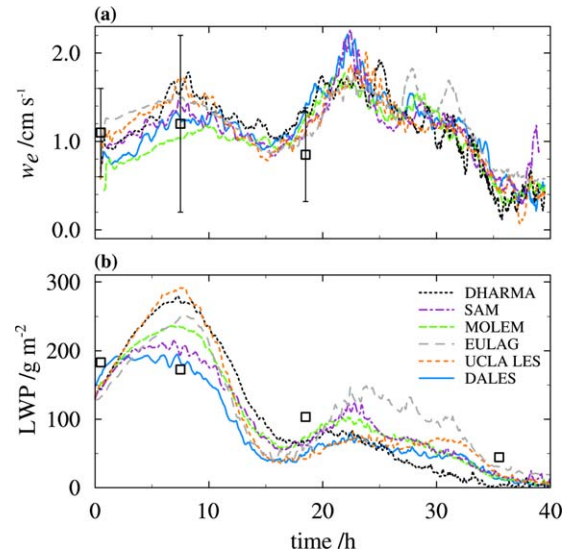

Figure 5. (a) The entrainment rate w_e and (b) the LWP as a function of time for the models indicated in the legend. Estimates based on observations of w_e including uncertainties were obtained from *De Roode and Duynkerke* [1997], while the values of the LWP where obtained by integrating the mean q_L profiles shown in Figure 7. A running averaging filter with a width of 1 h has been applied on the simulated entrainment rates.
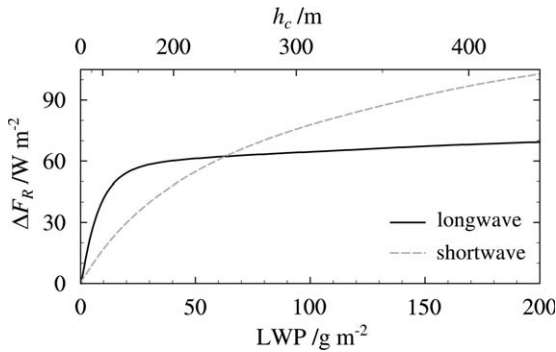
Figure 6. The difference in total longwave as well as shortwave radiative flux between the top and the base of an adiabatic stratocumulus cloud layer as a function of (bottom axis) LWP and (top axis) cloud thickness h_c. The radiative transfer code based on *Fu and Liou* [1993] that is used in DALES and UCLA LES was used to perform the calculations. By varying the total humidity in the mixed layer, $q_{T,\mathrm{ml}}$ in equation (1), different values for the LWP were obtained. The solar radiation fluxes were calculated at local noon and a cloud droplet number density of $N_c = 100 \mathrm{\ cm}^{-3}$ was used.

cause of the significant intermodel spread in the entrainment rate that is present during the initial 10 h.

[29] The inclusion of precipitation is also an important cause of the decreased entrainment rate as compared to the GCSS model intercomparison study based on ASTEX flight 3 (hour 8), in which microphysical processes were not taken into account [*Duynkerke et al.*, 1999]. The reported average entrainment rate of about 1.9 cm s^{-1} for those simulations was recognized to be high compared to the observed value of about 1.2 cm s^{-1}. The average entrainment rate presented here is, at about 1.4 cm s^{-1}, much better in line with the observations. Another contribution to this decrease of the entrainment rate comes from the use of interactive radiation schemes. These schemes produce a slight warming at cloud base that was not accounted for by the idealized longwave radiation parameterization schemes in the previous model intercomparisons. A final cause for the decrease is the higher vertical resolution of 5 m as compared to the 25 m resolution used by *Duynkerke et al.* [1999]. *Yamaguchi and Randall* [2012] showed that stratocumulus simulations benefit from even higher resolutions. The current resolution however, which is necessary to properly resolve the large gradient in the inversion layer, already limits the maximum time step of integration to less than 1 s. Using an even higher resolution in combination with the 40 h duration would make the simulation of the entire transition computationally too demanding. Based on the results of *Yamaguchi and Randall* [2012], the expected error in the entrainment rate due to the limited resolution is of the order of several percent. The deepening rate of the boundary layer, which is governed by the entrainment and the prescribed large-scale subsidence, is in a good agreement with the observations.

[30] Figure 5b shows the LWP, which is defined as:

$$\mathrm{LWP} = \int_0^\infty \rho_a q_L \mathrm{d}z. \qquad (6)$$

Note that q_L includes rain water. Estimates derived from the measured average liquid water specific humidity profiles are indicated by squares. The models show a steady or even increasing LWP during the first night, despite the boundary layer decoupling evident in Figure 4. Approximately 8 h after the start of the simulation the sun rises and the LWP decreases to a local minimum approximately 2–3 h after local noon. It is also evident that the large spread in the modeled LWP of over 100 gm^{-2} found during the first night is reduced significantly during daytime. An important reason explaining this LWP convergence is the fact that thicker clouds tend to absorb more solar radiation. This effect is illustrated in Figure 6, which shows the difference in both the total shortwave and longwave radiative fluxes between cloud top and cloud base as a function of LWP for an idealized, vertically well-mixed stratocumulus layer with a cloud droplet number density $N_c = 100$ cm^{-3}. During daytime, stratocumulus clouds with a higher LWP will absorb more solar radiation causing a stronger cloud thinning tendency.

[32] Figure 6 also shows that for LWP > 25 gm^{-2} the total longwave radiative flux divergence across the cloud layer becomes almost independent of LWP. For smaller LWP values the cloud layer becomes optically thin yielding a reduction in the emission as well as the absorption of longwave radiation. As an elevated source of negative buoyancy, longwave radiative cooling at the stratocumulus cloud top drives the vertical mixing. We notice from the DHARMA simulation results that after the LWP drops below 25 g m^{-2} around hour 30, the cloud cover quickly reduces to about 5–10%. This indicates that the decrease of longwave radiative cooling in combination with continued entrainment causes the stratocumulus layer to dissolve and break up. It furthermore shows that in this case the moisture input from the subcloud layer by cumuli is insufficient to maintain the cloud layer.

3.2. Mean State Vertical Profiles

[33] Hourly averaged LES results at selected times are next compared with observations gathered during flights 2–5 of the ASTEX Lagrangian experiment (see Table 3). The mean state of the atmosphere was calculated by bin averaging all measurements collected during horizontal, profiling and porpoising legs of the

Table 3. Summary of the Flight Details[a]

Number	Code	UTC Time (Date)	Simulation Time
1	RF05	1719–2133 (12 Jun)	
2	A209	0032–0426 (13 Jun)	Initialization
3	RF06	0451–1013 (13 Jun)	8th hour average
4	RF07	1627–2109 (13 Jun)	19th hour average
5	A210	1111–1302 (14 Jun)	36th hour average

[a]For more information, see *De Roode and Duynkerke* [1997, Table 1].

respective flights over height intervals of 100 m and the standard deviation of each of the bins was calculated.

[34] Figure 7 compares the aircraft observations with domain-averaged vertical profiles of thermodynamic state variables q_T, θ_L and q_L as well as the horizontal wind components u and v. The bin-averaged measurements are indicated by squares and the ± 1 standard deviation range of each bin is shown by error bars. We first notice that the modeled temperature and specific humidity in the free atmosphere agree well with the observations, suggesting realistic forcing tendencies due to radiation and large-scale subsidence. Moreover, the changes of the horizontal velocities u and v in time are close to those observed. Unfortunately, no measurements above 1800 m were collected during the last flight (hour 36).

[35] During the first half of the transition the simulated temperature and humidity profiles in the boundary layer agree well with the observations, with maximum humidity and temperature differences staying within 1 g kg^{-1} and 1 K, respectively. Considering the complexity of the case, the diversity of parameterization schemes used in the models and the relatively long simulation time this agreement between the models and observations is very encouraging.

[36] The simulated bulk evolution of the boundary layer profiles shows great similarity with the conceptual model of the vertical structure of decoupled boundary layers as proposed by *Wood and Bretherton* [2004, Figure 1]. Starting from a relatively shallow, well-mixed boundary layer, gradually a three-layered structure develops as the boundary layer deepens. Both the subcloud at the bottom of the boundary layer and the stratocumulus layer at the top are relatively well mixed and connected by a cumulus layer. The bulk of the turbulent transport through this layer is governed by few cumulus updrafts. Without exception, the models reproduce this change of the boundary layer structure very well.

[37] We notice some difference between model results and observations in the strength of the gradients of q_T and θ_L in the inversion layer during hours 8 and 19. This discrepancy could be due to the fact that the observations cover a much larger area including a larger spatial variability in the boundary layer height that cannot be represented in the rather limited horizontal LES domain. The result is that the simulated liquid water specific humidity profiles in Figures 7c and 7g have sharper peaks that are located more toward the top of the boundary layer as compared to the observed profiles.

[38] During the last flight the temperature and humidity differences between models and observations are significantly larger than during the first half of the transition. It should be noted that many of the legs during this flight were cloud free and significantly warmer and drier than the cloudy legs. Temperature excursions of the order of 1 K were measured over distances of more than 50 km. This mesoscale variability complicates the comparison of the models with the observations. Note that in the DHARMA model the upper part of the boundary layer becomes warmer after the relatively fast breakup of the stratocumulus layer than

in the other LES model results in which a solid stratocumulus cloud layer is maintained much longer. In the latter case longwave radiative loss at the top of the cloud layer causes a cooling tendency, which is significantly reduced when the cloud layer dissipates. Lastly, we note that high cirrus clouds were observed during the last flight. Their presence is neglected in the simulations, because their amount could not be estimated from the observations. However, as cirrus clouds increase the downwelling longwave radiation they actually reduce the cooling rate at the top of the cloud layer, which could partly explain the difference between the modeled and observed temperature.

3.3. Turbulence State Vertical Profiles

[39] The horizontal flight legs each with a length of about 60 km were used to calculate the turbulence statistics. Mesoscale fluctuations were filtered out by applying a running average with a length of 3.1 km [*De Roode and Duynkerke*, 1997]. The sampling error in the second-order moments is estimated to be about 20% for flights 3 and 4, and between 10 and 40% for flight 5.

[40] The turbulence state of the atmosphere during the flights is summarized by the profiles shown in Figure 8. It is clear from Figures 8a, 8d, and 8h that the observed gradual decrease of the horizontally averaged turbulent kinetic energy e in time is well reproduced by the models. As the transition progresses, the e profiles in both the models and the observations develop a minimum in the middle of the boundary layer. The profiles of the vertical velocity variance σ_w^2, which constitutes an important part of the turbulent kinetic energy, show this decreased turbulent mixing in the middle of the boundary layer more clearly, particularly during the second night (see Figure 8f). Only during the first night is a single peak in the vertical profile of σ_w^2 present, which indicates that the boundary layer remains relatively well mixed. Models that generate higher precipitation rates, for instance DALES and system for atmospheric modeling (SAM), also tend to have a lower vertical velocity variance and a more decoupled structure, which was also found by *Stevens et al.* [1998].

[41] The skewness of the vertical velocity S_w defined as:

$$S_w = \frac{\overline{w'^3}}{\sigma_w^3}, \tag{7}$$

increases steadily during the simulations. In the first part of the transition (Figure 8d), the negative skewness caused by downdrafts originating from the inversion almost completely cancels against the positive effect of updrafts from the surface, resulting in small values for S_w in the middle of the boundary layer. In the model simulations, updrafts seem to be more dominant in comparison to the observations. The large positive values for S_w shown in Figure 8l indicate the presence of rising cumulus clouds at the end of the transition. Their high upward velocities constitute the tail of the probability distribution of w which explains some of the intermodel spread in S_w.
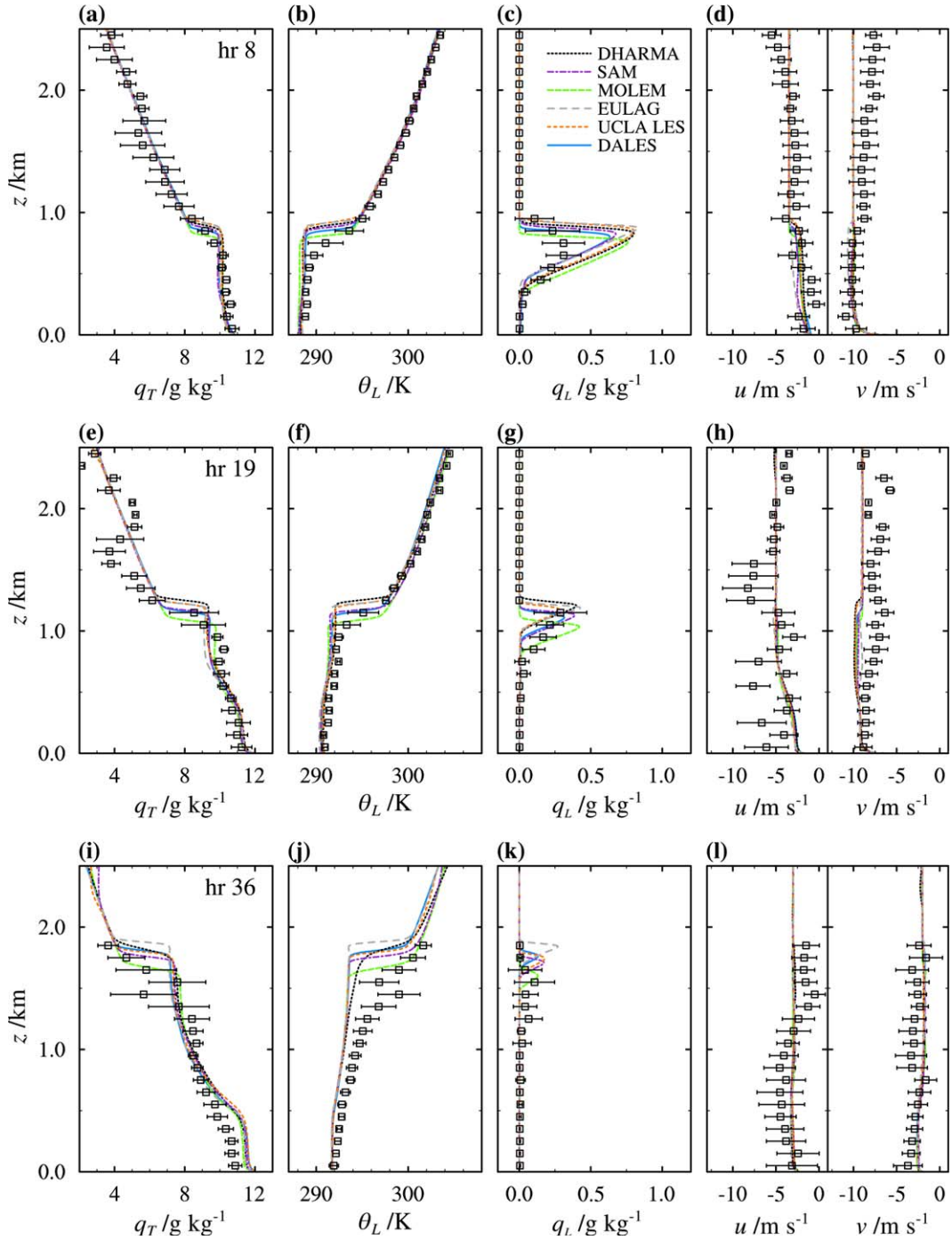
Figure 7. The domain averaged vertical profiles of the mean state variables q_T, θ_L, q_L, and the horizontal wind components u and v for ASTEX flights (a–d) 3, (e–h) 4, and (i–l) 5. Line styles and colors according to the legend. The black squares denote bin-averaged observations with the $\pm\sigma$ range indicated by the error bars.

[42] Throughout the simulations the virtual potential temperature flux $\overline{w'\theta_V'}$ is slightly negative at the top of the subcloud layer (see Figures 8c, 8g, and 8k). The linear vertical profile of $\overline{w'\theta_V'}$ and the approximately parabolic σ_w^2 profile in the subcloud layer suggest a strong similarity with the dynamic structure of the clear convective boundary layer [*Stevens et al.*, 2001]. This subcloud layer structure seems to be very robust in the model results and the agreement with the observations is striking. A negative value for $\overline{w'\theta_V'}$ indicates that rising thermals have a negative buoyancy that may prohibit them to rise further toward the stratocumulus layer. *Nicholls* [1984] and *Bretherton and Wyant* [1997] suggested that a subsequent decrease of vertical moisture transport out of the subcloud layer could result in a rapid thinning of the
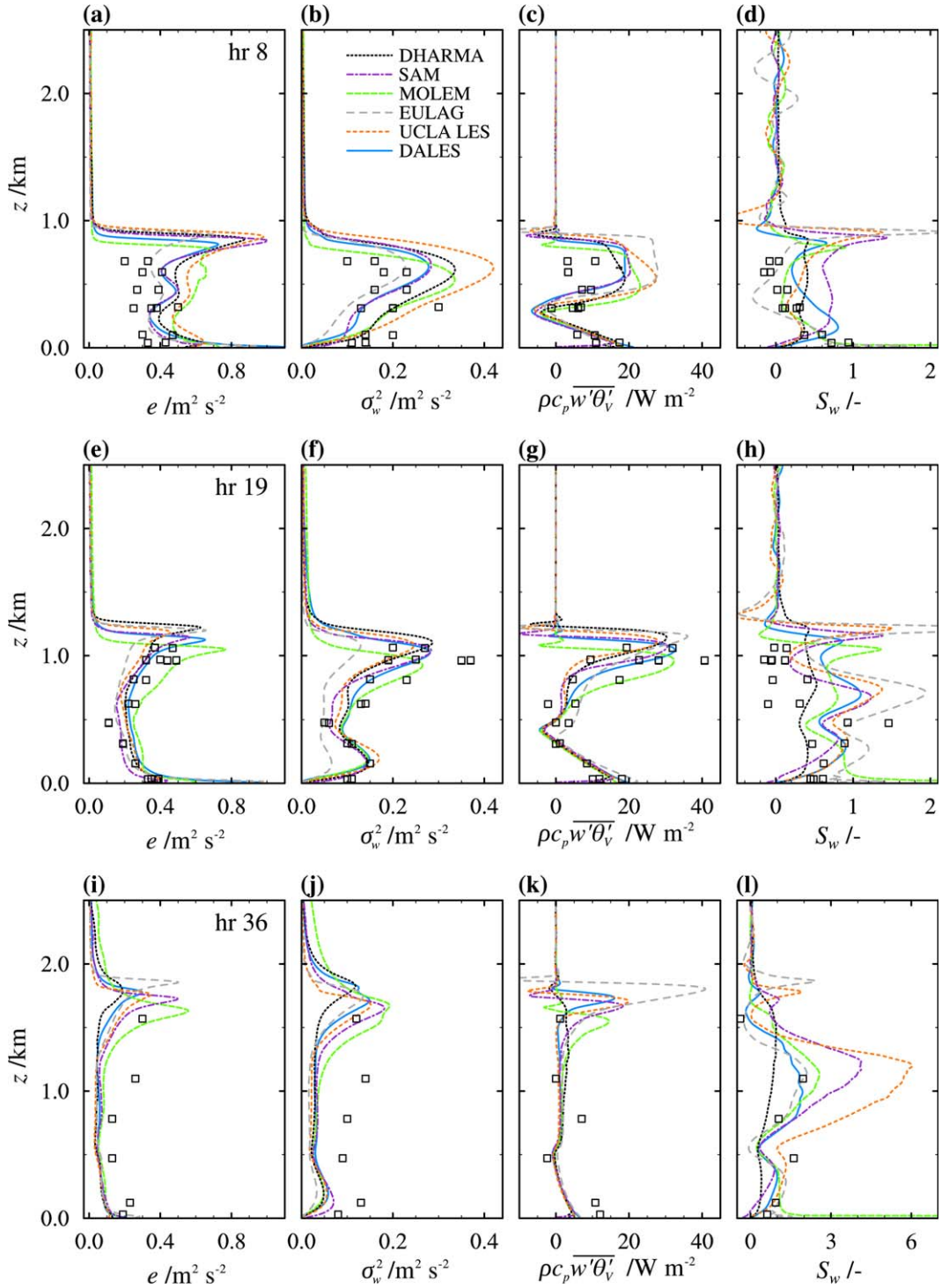
Figure 8. Vertical profiles of domain averaged turbulence statistics, the turbulent kinetic energy e, the vertical velocity variance σ_w^2, the virtual potential temperature flux $\overline{w'\theta_V'}$, and the vertical velocity skewness S_w, for ASTEX flights (a–d) 3, (e–h) 4, and (i–l) 5. Line styles and colors according to the legend. The black squares denote observations derived from measurement time series taken during horizontal flight legs. Note the different scale of the horizontal axis in Figure 8l.

stratocumulus cloud layer. The results for this transition, however, indicate that stratocumulus clouds can persist for a day or more even when the boundary layer is not well mixed.

[43] The buoyancy peak is located at the top of the stratocumulus cloud layer, where the virtual potential temperature flux can be written in terms of turbulent fluxes of θ_L and q_T as follows:
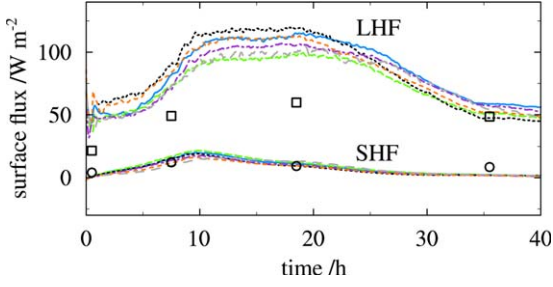
Figure 9. The surface fluxes of latent (upper set of lines and squares) and sensible heat (lower set and circles) as a function of time. Legend as in Figure 8. The observations are derived from the flight legs flown closest to the surface at approximately 30 m height, except for flight 2 for which the lowest available data were gathered at a height of approximately 160 m.

$$\overline{w'\theta_V'}_{\text{top}} = A_w \overline{w'\theta_L'}_{\text{top}} + B_w \overline{w'q_T'}_{\text{top}}. \quad (8)$$

[44] Here $A_w \approx 0.5$ and $B_w \approx 1000$ K are thermodynamic coefficients for a saturated environment. The subscripted "top" denotes variables at the top of the boundary layer just below the inversion. The turbulent flux of a conserved variable $\varphi \in \{q_T, \theta_L\}$ at the top of the boundary layer due to entrainment only can be approximated using the flux-jump relation [*Lilly*, 1968],

$$\overline{w'\varphi'}_{\text{ent}} = -w_e \Delta\varphi. \quad (9)$$

[45] Here Δ again denotes the difference between a variable just above and just below the inversion layer. Combining equations (8) and (9) the following can be written:

$$\overline{w'\theta_V'}_{\text{ent}} = -w_e(A_w \Delta\theta_L + B_w \Delta q_T). \quad (10)$$

[46] According this equation, the increase of the buoyancy flux between hours 8 and 19 can in the first place be attributed to the strengthening of the inversion jump of q_T from approximately -2 to -3 g kg^{-1} which is apparent from Figure 7. *Stevens et al.* [1998] furthermore found that precipitation tends to reduce the buoyancy flux. A second cause for the increase of $\overline{w'\theta_V'}_{\text{top}}$ is therefore the decrease of the precipitation rate between the mentioned hours.

4. Humidity Budget

[47] Following *Bretherton et al.* [1995], the humidity budget is analyzed next with a particular focus on the surface fluxes of latent heat and drizzle. Some additional sensitivity experiments will furthermore be discussed that have been performed in order to investigate the range of uncertainty resulting from the case setup.

4.1. Surface Latent Heat Flux

[48] Figure 9 shows time series of the modeled surface sensible (SHF) as well as the surface latent heat flux (LHF). The observed surface flux values shown in this figure were calculated from the flight legs performed in the surface layer at a height of about 30 m, except for flight 2 for which the lowest available data was gathered at a height of approximately 160 m. The results will be interpreted by means of the following bulk formula:

$$\overline{w'q_T'}|_0 = C_q |\mathbf{u}|_{\text{sl}} \{q_{\text{sat}}(T_s) - q_{T,\text{sl}}\}. \quad (11)$$

[49] Here C_q is the bulk transfer coefficient for moisture, $|\mathbf{u}|$ is the magnitude of the horizontal wind vector and $q_{\text{sat}}(T_s)$ is the saturation specific humidity for the temperature of the surface T_s. The subscripted "sl" denotes the surface layer. The surface LHF increases to approximately 100 W m^{-2} during the initial 10 h of the simulation owing to an increase in both the SST and the horizontal wind speed. By contrast, during the second part of the transition the LHF lowers to around 50 W m^{-2} due to a considerable decrease of the total wind speed (see Figure 2a).

[50] Despite the fact that close to the surface the modeled humidity and horizontal wind velocity agree well with the observations (Figure 7), the modeled surface LHF is much larger than in the observations. The reported uncertainty in the SST is about 0.5 K [*Bretherton et al.*, 1995], which corresponds to a saturation specific humidity uncertainty of 0.45 g kg^{-1} following Clausius-Clapeyron. This translates into an uncertainty of only 15% in the modeled surface flux assuming no other variables are influenced. The remaining variable in equation (11) is the bulk transfer coefficient for moisture C_q. This transfer coefficient is determined among others from the surface roughness length z_0, which is prescribed to be constant at 0.2 mm. This value is typically used for open sea conditions. However, z_0 is actually determined by the wave height, which in turn is a function of the horizontal wind velocity close to the surface. This effect is described by the Charnock relation,

$$z_0 = \frac{\alpha_c u_*^2}{g}, \quad (12)$$

in which u_* is the friction velocity, g is gravitational acceleration and α_c is the Charnock parameter. The value of α_c varies significantly among models: $0.011 \lesssim \alpha_c \lesssim 0.018$ [*Renfrew et al.*, 2002]. A test was performed with DALES in which the Charnock relation was used to determine z_0, in order to assess the effect of this variable roughness length on the surface LHF. Using a typical value $\alpha_c = 0.015$ results in $z_0 \approx 0.16$ mm during the first 20 h of the simulation, which is somewhat lower than the prescribed constant value of 0.2 mm that was used for the reference simulation. In the second half of the transition, z_0 decreases steadily to about 0.03 mm. The lower z_0 causes a decrease of the surface LHF throughout the transition of about 15% as compared to the reference simulation. However, it has no significant effect on the LWP or on the timing of stratocumulus cloud breakup.
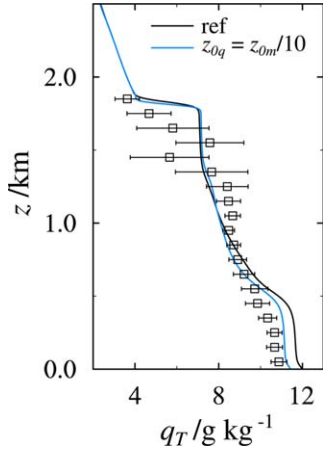
Figure 10. Horizontally averaged q_T profiles for the reference simulation (black) as well as the simulation with $(z_{0q}, z_{0h}) = z_{0m}/10 = 0.02$mm (blue) at hour 36 of the simulation.

[51] Apart from Charnock's relation, SCMs often use a lower value of the surface roughness length for moisture and heat than for momentum (see also *Vickers and Mahrt* [2010], for observational evidence). Therefore, an additional test was performed in which the value of z_0 for humidity and heat was one tenth that for momentum: $z_{0q,h} = z_{0m}/10$. Again, a reduction of the LHF of about 10–15% was found. In Figure 10, the humidity profile of this test is compared with the reference simulation. Clearly, the decrease of the surface roughness length causes the humidity in the subcloud layer to decrease by about 0.5 g kg^{-1}, which is in better agreement with the observations than the results of the reference simulation. The humidity in the cloud layer remains virtually unaffected.

4.2. Moisture Flux at Stratocumulus Cloud Base

[52] Figure 11 clearly shows that the modeled turbulent humidity fluxes in the subcloud layer are systematically larger than observed. In the cloud layer, the collected high-frequency humidity measurements have a large error [*Wang and Lenschow*, 1995]. More accurate humidity measurements from a different instrument are available, but the sampling frequency of 1 Hz is too low to yield accurate flux estimates. However, an estimate of the magnitude of $\overline{w'q_T'}$ in the stratocumulus layer can be obtained from the observed $\overline{w'\theta_V'}$ and $\overline{w'\theta_L'}$ fluxes using equation (8). Using for example the observations from flight 4, this method gives a maximum value of about 100 W m^{-2} at the top of the boundary layer. These estimates therefore suggest that the observations of $\overline{w'q_T'}$ in the cloud layer that are shown in Figure 11 are probably too high.

[53] Despite the fact that the buoyancy flux at the top of the subcloud layer is significantly negative throughout the simulations (Figure 8), the vertical variations in the simulated turbulent vertical humidity fluxes are very small in the subcloud layer. This indicates that much of the moisture evaporating from the surface is transported to the cloud layer. As such, the modeled flux profiles do not exhibit the strongly decoupled structure with humidity fluxes going to zero at the top of the subcloud layer as suggested in early studies by *Nicholls* [1984] or *Bougeault* [1985]. To quantify how much moisture actually is transported from the subcloud to the stratocumulus cloud layer and how this amount relates to the surface evaporation we define the quantity r_{q_T} which gives the ratio of the moisture flux at the mean cloud base z_b over the flux at the surface:

$$r_{q_T} = \frac{\overline{w'q_T'}(z_b)}{\overline{w'q_T'}(0)}. \qquad (13)$$

[54] A clear diurnal cycle in r_{q_T} is visible in Figure 12, with values exceeding unity during the night and a
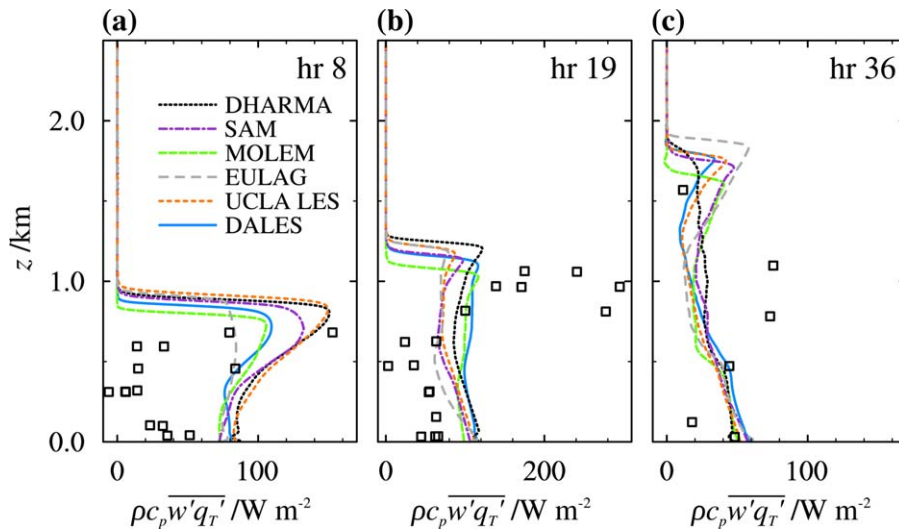

Figure 11. Domain averaged profiles of the turbulent humidity flux $\overline{w'q_T'}$ for the hours corresponding to flights (a) 3, (b) 4, and (c) 5. The black squares denote observations. Note the different scale of the horizontal axis in Figure 11b.
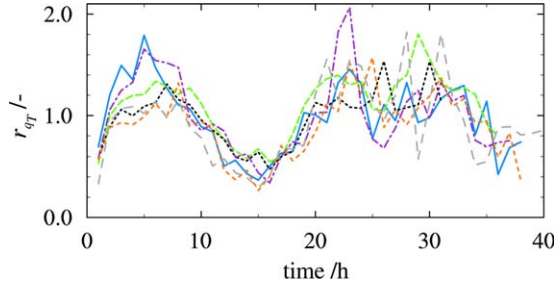
Figure 12. The ratio r_{q_T} of the humidity flux at mean cloud base z_b to the surface flux as defined in equation (13). Legend as in Figure 11. The series are cut off as soon as the average cloud cover drops below 0.95.

distinct minimum during the first day. This suggests that the decoupling of the boundary layer is much more effective in reducing the upward moisture transport to the stratocumulus cloud layer during the day than for nighttime conditions. It is interesting to note that during the first day of the transition the model mean value of r_{q_T} is about 0.95, which suggests a near zero divergence of the moisture flux for the ASTEX subcloud layer.

4.3. Precipitation

[55] The surface precipitation flux as a function of time is shown in Figure 13b. This flux is relatively large during the first night, with domain averaged values of up to 30 W m^{-2} (≈ 1 mm day^{-1}). Surface precipitation rates rapidly drop to zero as the cloud layer thins during the day. The observed and modeled precipitation rates are significantly different, particularly at hours 8 and 19, which raises questions about the observations, as we will now show. For comparison we also calculated the precipitation rate at cloud base from a relation between the LWP and the cloud droplet number density N_c based on observations [Comstock et al., 2004],

$$\rho L_v F_p(z_b) = 10.8 \left(\frac{\text{LWP}}{N_c} \right)^{1.75}. \tag{14}$$

[56] Here $\left(\rho L_v F_p \right)$, LWP and N_c are in W m^{-2}, g m^2, and cm^{-3}, respectively. Geoffroy et al. [2008] give a thorough overview of drizzle parameterizations, which includes a similar relation by vanZanten et al. [2005]. That relation is found to give almost identical results as the one from Comstock et al. [2004] presented in Figure 13a. The model results and direct observations (squares) are also shown in this figure. The error bars span the range of observed droplet number densities $N_c = 50 - 150$ cm^{-3} (respectively the upper and lower bounds) as reported by Bretherton and Pincus [1995]. The results calculated using the parameterization of equation (14) show a trend that is consistent with the LES results and hint at an overestimation of the precipitation rates as diagnosed from the observations.

[57] During the first hours of the simulations there are significant intermodel differences in the precipita-

tion rates. Models that are less prone to produce rain allow the LWP to grow during the first night (compare Figure 5). These models also start producing rain as the LWP increases. All models eventually have similar precipitation rates around hour 10, but at different values of the LWP.

[58] Figure 14 shows a clear correlation between the precipitation rate at stratocumulus cloud base and the LWP, both of which are averages of the model results during the first 12 h of the simulation. Additional simulations were performed with DALES, using $N_c = 60$, 100 (reference), and 200 cm^{-3}. These cases were run using two microphysics schemes: the scheme by Khairoutdinov and Kogan [2000, KK00 hereafter], which was used for the reference simulation, and the scheme of Seifert and Beheng [2001, SB01 hereafter]. The top axis of the Figure 14 shows a rough indication of the LWP tendency due to the removal of liquid water by precipitation only:

$$\left[\frac{\text{dLWP}}{\text{d}t} \right]_{\text{driz}} = - \frac{F_p(z_b)}{L_v} \tag{15}$$

in units of g m^{-2} h^{-1}. Note that the effect of evaporation of precipitation below cloud base is neglected in this tendency. The estimated LWP difference between for instance the University of California, Los Angeles (UCLA) LES and DALES results over the 12 h period is approximately 250 g m^{-2}. A secondary effect of a higher precipitation rate is a decrease of the
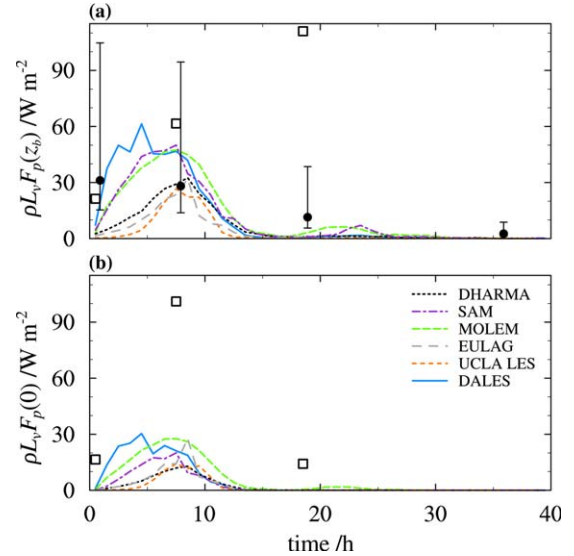

Figure 13. The precipitation rate F_p in units of W m^{-2} (a) at mean cloud base height z_b and (b) at the surface for the models denoted in the legend. Squares denote average precipitation rates obtained from the flight legs that were flown closest to the mentioned levels. The black dots show parameterized precipitation rates at z_b calculated using equation (14) with a cloud droplet number concentration $N_c = 100$ cm^{-3}, while the error bars indicate the range of precipitation rates spanned using $N_c = 50$ and 150 cm^{-3}.

495

entrainment rate as was already shown by *Nicholls* [1984] and *Chen and Cotton* [1987] among others. *Ackerman et al.* [2004] therefore argue that the LWP response to increased precipitation is the result of the competition between the increased removal of liquid water from the boundary layer and the reduced drying due to the lower entrainment rate. The free atmosphere was relatively moist during ASTEX, such that the former response is dominant.

[59] Figure 15 shows that the average entrainment rate indeed decreases with increased precipitation rate. It is striking to see that the model results exhibit this strong correlation between the precipitation rate at cloud base and the entrainment rate considering the multitude of processes through which microphysics impact on the boundary layer dynamics [*Ackerman et al.*, 2009]. The scatter plots shown in Figures 14 and 15 furthermore suggest that the significant spread noted in the modeled LWP and entrainment rates during the first 12 h is mainly attributable to the differences among the microphysics parameterization schemes.

[60] The simulation results nevertheless indicate that the pace of the transition is hardly related to the microphysical details of the models. SAM, met office large eddy model (MOLEM), UCLA LES, and DALES all predict the breakup of the stratocumulus cloud layer at approximately the same time (see Figure 4), despite their strongly varying precipitation rates. This is basically due to the strong decrease of the LWP during the
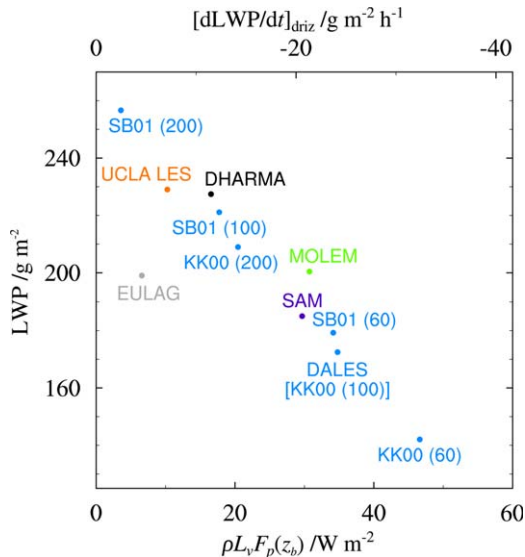

Figure 15. As Figure 14, but here for the entrainment rate w_e.

first day. The thin veil of stratocumulus cloud at the top of the boundary layer that remains after this first day does not support significant amounts of precipitation, such that the LWP and entrainment differences among the models stay relatively small for the remainder of the transition.

5.   Discussion and Conclusions

[61] In this study the stratocumulus transition as observed during the ASTEX field experiment is simulated by six different LES models. Despite the complexity of the case, including multiple time-varying boundary conditions, a diurnally varying interactive radiative forcing, the inclusion of parameterized microphysical processes and the long simulation time of 40 h, the model results agree remarkably well with the aircraft observations. In particular, the models are able to closely reproduce the evolution of a vertically well-mixed stratocumulus-topped boundary layer to a much deeper decoupled boundary layer with shallow cumulus clouds penetrating stratocumulus above. Particular features of the observed turbulence structure, such as the strong increase of the buoyancy flux at the top of the boundary layer and the development of a double-peaked vertical velocity variance profile, are also well captured by the models.

[62] The ratio of the turbulent humidity flux at the stratocumulus cloud base to the surface evaporation flux is shown to exhibit a distinct diurnal cycle. It exceeds unity during the night implying a net drying of the subcloud layer and moistening during the day. This also indicates that during the night the cumulus clouds are much more efficient in feeding the stratocumulus cloud layer with moisture from the subcloud layer than during daytime [*Martin et al.*, 1995; *Chung et al.*, 2012].

[63] The largest source of spread among the models is arguably due to the parameterization of microphysical

Figure 14. Scatter plot of the time averaged LWP as a function of time averaged precipitation rate at stratocumulus cloud base, both of which are averages of the model results during the first 12 h of the transition. The top axis shows the precipitation rate in terms of a LWP tendency in g m^{-2} h^{-1} as given by equation (15). The labels indicate the model or the microphysics scheme (in DALES) used, while the numbers between the parentheses indicate the cloud droplet number density in cm^{-3}.
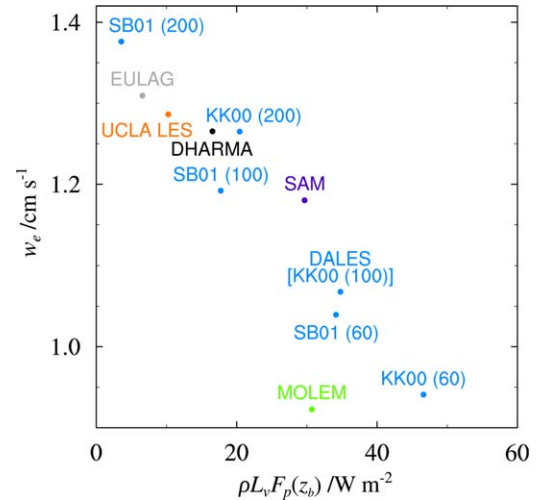
processes. In particular, additional sensitivity simulations using DALES indicate that the precipitation flux is reduced by about 50% if the microphysics scheme is changed from the one proposed by *Khairoutdinov and Kogan* [2000] to *Seifert and Beheng* [2001]. The substantial differences in LWP (exceeding 100 g m^{-2}) and entrainment rate (about 0.3 cm s^{-1}) among the models during the first night are shown to be strongly related to the magnitude of the precipitation flux at stratocumulus cloud base. Unfortunately, the uncertainty in the precipitation rates derived from the observations is too large to conclude which microphysics scheme should be preferred over another. Specifically, a comparison of the ASTEX observed drizzle rates with results from a parameterization based on a careful analysis of more recent field observations by *Comstock et al.* [2004] shows that the former are much larger. The differences that emerge in the modeled LWPs during the first night are diminished during daytime because clouds with a high LWP tend to absorb more radiation and therefore evaporate more liquid water. During the subsequent night the cloud layer is too thin to maintain significant drizzle rates.

[64] As the values for the surface roughness length for scalars like moisture and heat used by the LES models are higher than the typical values used in climate and weather forecast models, a sensitivity test was performed using DALES. This simulation shows that a reduction of the roughness length for scalars by a factor of 10 results in a reduction of the surface latent heat flux by about 15%, which however does not significantly affect the timing of cloud breakup. The subcloud humidity at the end of the transition is approximately 0.5 g kg^{-1} lower than for the reference simulation and is in better agreement with the observations. This result therefore suggests that for this study a smaller value of the surface roughness length for scalars would be more appropriate for LES models than the value that was originally proposed.

[65] At the end of the transition the observed temperature in the stratocumulus cloud layer is significantly higher than in the simulations. The cold bias in the modeling results might be partly due to the observed appearance of cirrus clouds. Their effect on the longwave radiative cooling at the stratocumulus cloud top has been neglected in the simulations, because the precise amount of these high clouds could not be derived from the aircraft observations. The LES models furthermore used a rather small horizontal domain such that mesoscale organization of clouds could not be captured. Careful inspection of the aircraft observations shows significant mesoscale fluctuations, with lower temperatures in the stratocumulus-topped cloud layers as compared to the surrounding clear areas.

[66] The results of this research show that much progress has been made in the modeling of stratocumulus transitions since the previous intercomparison cases based on ASTEX [*Duynkerke et al.*, 1999; *Bretherton et al.*, 1999]. This progress is mainly attributable to the availability of sufficient computational power to perform the required multiday simulations using a three-dimensional LES model at high resolution instead of one- or two-dimensional turbulence models. Other important improvements are the incorporation of advanced parameterization schemes for radiation and precipitation as well as the use of prescribed SSTs instead of the prescribed surface flux forcing used in the previous LES intercomparison studies based on flights 2 and 3 of the first Lagrangian.

[67] In contrast to the aircraft observations, the LES model results now provide a continuous and internally consistent representation of the stratocumulus transition that took place during the ASTEX first Lagrangian. Furthermore, the LESs give the opportunity to evaluate the performance of specific parameterization schemes by providing detailed information such as mass flux statistics that is difficult to obtain from observations. This makes these results valuable as a benchmark for the evaluation and further development of parameterizations schemes of SCMs within the GCSS strategy [*Randall et al.*, 2003].

References

Abel, S. J., and B. J. Shipway (2007), A comparison of cloud-resolving model simulations of trade wind cumulus with aircraft observations taken during RICO, *Q. J. R. Meteorol. Soc.*, *133*(624), 781–794.

Ackerman, A. S., M. P. Kirkpatrick, D. E. Stevens, and O. B. Toon (2004), The impact of humidity above stratiform clouds on indirect aerosol climate forcing, *Nature*, *432*(7020), 1014–1017.

Ackerman, A. S., et al. (2009), Large-eddy simulations of a drizzling, stratocumulus-topped marine boundary layer, Mon. *Weather Rev.*, *137*(3), 1083–1110.

Albrecht, B. A., C. S. Bretherton, D. Johnson, W. H. Scubert, and A. S. Frisch (1995), The Atlantic stratocumulus transition experiment—ASTEX, *Bull. Am. Meteorol. Soc.*, *76*(6), 889–904.

Blossey, P. N., and D. R. Durran (2008), Selective monotonicity preservation in scalar advection, *J. Comput. Phys.*, *227*(10), 5160–5183.

Bougeault, P. (1985), The diurnal cycle of the marine stratocumulus layer: A higher-order model study, *J. Atmos. Sci.*, *42*(24), 2826–2843.

Bretherton, C. S., and R. Pincus (1995), Cloudiness and marine boundary layer dynamics in the ASTEX lagrangian experiments. Part I: Synoptic setting and vertical structure, *J. Atmos. Sci.*, *52*(16), 2707–2723.

Bretherton, C. S., and M. C. Wyant (1997), Moisture transport, lower-tropospheric stability, and decoupling of cloud-topped boundary layers, *J. Atmos. Sci.*, *54*(1), 148–167.

Bretherton, C. S., P. Austin, and S. T. Siems (1995), Cloudiness and marine boundary layer dynamics in the ASTEX lagrangian experiments. Part II: Cloudiness, drizzle, surface fluxes, and entrainment, *J. Atmos. Sci.*, *52*(16), 2724–2735.

Bretherton, C. S., S. K. Krueger, M. C. Wyant, P. Bechtold, E. Van Meijgaard, B. Stevens, and J. Teixeira (1999), A GCSS boundary-layer cloud model intercomparison study of the first ASTEX Lagrangian experiment, *Boundary Layer Meteorol.*, *93*(3), 341–380.

Bretherton, C. S., T. Uttal, C. W. Fairall, S. E. Yuter, R. A. Weller, D. Baumgardner, K. Comstock, R. Wood, and G. B. Raga (2004), The

EPIC 2001 stratocumulus study, *Bull. Am. Meteorol. Soc.*, *85*(7), 967–977.

Briegleb, B. P. (1992), Delta-Eddington approximation for solar radiation in the NCAR community climate model, *J. Geophys. Res.*, *97*(D7), 7603–7612.

Chen, C., and W. R. Cotton (1987), The physics of the marine stratocumulus-capped mixed layer, *J. Atmos. Sci.*, *44*(20), 2951–2977.

Chlond, A., and A. Wolkau (2000), Large-eddy simulation of a nocturnal stratocumulus-topped marine atmospheric boundary layer: An uncertainty analysis, Boundary-Layer Meteorology, *95*(1), 31–55.

Chung, D., G. Matheou, and J. Teixeira (2012), Steady-state large-eddy simulations to study the stratocumulus to shallow cumulus cloud transition, *J. Atmos. Sci.*, *69*(11), 3264–3276.

Ciesielski, P. E., W. H. Schubert, and R. H. Johnson (1999), Large-scale heat and moisture budgets over the ASTEX region, *J. Atmos. Sci.*, *56*(18), 3241–3261.

Ciesielski, P. E., W. H. Schubert, and R. H. Johnson (2001), Diurnal variability of the marine boundary layer during ASTEX, *J. Atmos. Sci.*, *58*(16), 2355–2376.

Comstock, K. K., R. Wood, S. E. Yuter, and C. S. Bretherton (2004), Reflectivity and rain rate in and below drizzling stratocumulus, *Q. J. R. Meteorol. Soc.*, *130*(603), 2891–2918.

De Roode, S. R., and P. G. Duynkerke (1997), Observed lagrangian transition of stratocumulus into cumulus during ASTEX: Mean state and turbulence structure, *J. Atmos. Sci.*, *54*(17), 2157–2173.

De Roode, S. R., and J. J. van der Dussen (2010), Large-eddy simulation of a stratocumulus to cumulus cloud transition as observed during ASTEX, paper presented at 19th Symposium on Boundary Layers and Turbulence, American Meteorological Society (AMS), Keystone, Colo.

De Roode, S. R., I. Sandu, J. J. van der Dussen, A. S. Ackerman, P. N. Blossey, A. Lock, A. P. Siebesma, and B. Stevens (2012), LES results of the EUCLIPSE Lagrangian stratocumulus to shallow cumulus transition cases, paper presented at 20th Symposium on Boundary Layers and Turbulence, American Meteorological Society (AMS), Boston, Mass.

Duynkerke, P. G., P. J. Jonker, A. Chlond, M. C. Van Zanten, J. Cuxart, P. Clark, E. Sanchez, G. Martin, G. Lenderink, and J. Teixeira (1999), Intercomparison of three- and one-dimensional model simulations and aircraft observations of stratocumulus, *Boundary Layer Meteorol.*, *92*(3), 453–487.

Edwards, J. M., and A. Slingo (1996), Studies with a flexible new radiation code. I: Choosing a configuration for a large-scale model, *Q. J. R. Meteorol. Soc.*, *122*(531), 689–719.

Fu, Q., and K. N. Liou (1993), Parameterization of the radiative properties of cirrus clouds, *J. Atmos. Sci.*, *50*(13), 2008–2025.

Geoffroy, O., J.-L. Brenguier, and I. Sandu (2008), Relationship between drizzle rate, liquid water path and droplet concentration at the scale of a stratocumulus cloud system, *Atmos. Chem. Phys.*, *8*(16), 4641–4654.

Heus, T., et al. (2010), Formulation of the Dutch atmospheric large-eddy simulation (DALES) and overview of its applications, *Geosci. Model Dev.*, *3*(2), 415–444.

Khairoutdinov, M., and Y. Kogan (2000), A new cloud physics parameterization in a large-eddy simulation model of marine stratocumulus, *Mon. Weather Rev.*, *128*(1), 229–243.

Khairoutdinov, M. F., and D. A. Randall (2003), Cloud resolving modeling of the ARM summer 1997 IOP: Model formulation, results, uncertainties, and sensitivities, *J. Atmos. Sci.*, *60*(4), 607–625.

Klein, S. A., and D. L. Hartmann (1993), The seasonal cycle of low stratiform clouds, *J. Clim.*, *6*(8), 1587–1606.

Krueger, S. K., G. T. McLean, and Q. Fu (1995), Numerical simulation of the stratus-to-cumulus transition in the subtropical marine boundary layer. Part I: Boundary-layer structure, *J. Atmos. Sci.*, *52*(16), 2839–2850.

Lilly, D. K. (1968), Models of cloud-topped mixed layers under a strong inversion, *Q. J. R. Meteorol. Soc.*, *94*(401), 292–309.

Martin, G. M., D. W. Johnson, D. P. Rogers, P. R. Jonas, P. Minnis, and D. A. Hegg (1995), Observations of the interaction between cumulus clouds and warm stratocumulus clouds in the marine boundary layer during ASTEX, *J. Atmos. Sci.*, *52*(16), 2902–2922.

Mlawer, E. J., S. J. Taubman, P. D. Brown, M. J. Iacono, and S. A. Clough (1997), Radiative transfer for inhomogeneous atmospheres:

RRTM, a validated correlated-k model for the longwave, *J. Geophys. Res.*, *102*(D14), 16,663–16,682.

Morrison, H., J. A. Curry, and V. I. Khvorostyanov (2005), A new double-moment microphysics parameterization for application in cloud and climate models. Part I: Description, *J. Atmos. Sci.*, *62*(6), 1665–1677.

Nicholls, S. (1984), The dynamics of stratocumulus: Aircraft observations and comparisons with a mixed layer model, *Q. J. R. Meteorol. Soc.*, *110*(466), 783–820.

Pawlowska, H., and J.-L. Brenguier (2000), Microphysical properties of stratocumulus clouds during ACE-2, *Tellus, Ser. B*, *52*(2), 868–887.

Pincus, R., and B. Stevens (2009), Monte Carlo spectral integration: A consistent approximation for radiative transfer in large eddy simulations, *J. Adv. Model. Earth Syst.*, *1*, 1, doi:10.3894/JAMES.2009.1.1.

Prusa, J. M., P. K. Smolarkiewicz, and A. A. Wyszogrodzki (2008), EULAG, a computational model for multiscale flows, *Comput. Fluids*, *37*(9), 1193–1207.

Randall, D., et al. (2003), Confronting models with data: The GEWEX cloud systems study, *Bull. Am. Meteorol. Soc.*, *84*(4), 455–469.

Renfrew, I. A., G. W. K. Moore, P. S. Guest, and K. Bumke (2002), A comparison of surface layer and surface turbulent flux observations over the Labrador sea with ECMWF analyses and NCEP reanalyses, *J. Phys. Oceanogr.*, *32*(2), 383–400.

Sandu, I., and B. Stevens (2011), On the factors modulating the stratocumulus to cumulus transitions, *J. Atmos. Sci.*, *68*(9), 1865–1881.

Sandu, I., B. Stevens, and R. Pincus (2010), On the transitions in marine boundary layer cloudiness, *Atmos. Chem. Phys.*, *10*(5), 2377–2391, doi:http://dx.doi.org/10.5194/acp-10-2377-2010.

Seifert, A., and K. D. Beheng (2001), A double-moment parameterization for simulating autoconversion, accretion and selfcollection, *Atmos. Res.*, *59-60*, 265–281.

Shutts, G. J., and M. E. B. Gray (1994), A numerical modelling study of the geostrophic adjustment process following deep convection, *Q. J. R. Meteorol. Soc.*, *120*(519), 1145–1178.

Sigg, R., and G. Svensson (2004), Three-dimensional simulation of the ASTEX Lagrangian 1 field experiment with a regional numerical weather prediction model, *Q. J. R. Meteorol. Soc.*, *130*(597), 707–724.

Smolarkiewicz, P. K. (2006), Multidimensional positive definite advection transport algorithm: An overview, *Int. J. Numer. Methods Fluids*, *50*(10), 1123–1144.

Smolarkiewicz, P. K., and W. W. Grabowski (1990), The multidimensional positive definite advection transport algorithm: Nonoscillatory option, *J. Comput. Phys.*, *86*(2), 355–375.

Stevens, B., and A. Seifert (2008), Understanding macrophysical outcomes of microphysical choices in simulations of shallow cumulus convection, *J. Meteorol. Soc. Jpn.*, *86A*, 143–162.

Stevens, B., W. R. Cotton, G. Feingold, and C.-H. Moeng (1998), Large-eddy simulations of strongly precipitating, shallow, stratocumulus-topped boundary layers, *J. Atmos. Sci.*, *55*(24), 3616–3638.

Stevens, B., et al. (2001), Simulations of trade wind cumuli under a strong inversion, *J. Atmos. Sci.*, *58*(14), 1870–1891.

Stevens, B., et al. (2005), Evaluation of large-eddy simulations via observations of nocturnal marine stratocumulus, *Mon. Weather Rev.*, *133*(6), 1443–1462.

Stevens, D. E., and S. Bretherton (1996), A forward-in-time advection scheme and adaptive multilevel flow solver for nearly incompressible atmospheric flow, *J. Comput. Phys.*, *129*(2), 284–295.

Stevens, D. E., A. S. Ackerman, and C. S. Bretherton (2002), Effects of domain size and numerical resolution on the simulation of shallow cumulus convection, *J. Atmos. Sci.*, *59*(23), 3285–3301.

Svensson, G., M. Tjernström, and D. Koračin (2000), The sensitivity of a stratocumulus transition: Model simulations of the ASTEX first Lagrangian, *Boundary Layer Meteorol.*, *95*(1), 57–90.

Teixeira, J., et al. (2011), Tropical and subtropical cloud transitions in weather and climate prediction models: The GCSS/WGNE pacific cross-section intercomparison (GPCI), *J. Clim.*, *24*(20), 5223–5256.

Toon, O. B., C. P. McKay, T. P. Ackerman, and K. Santhanam (1989), Rapid calculation of radiative heating rates and photodissociation rates in inhomogeneous multiple scattering atmospheres, *J. Geophys. Res.*, *94*(D13), 16,287–16,301.

vanZanten, M. C., B. Stevens, G. Vali, and D. H. Lenschow (2005), Observations of drizzle in nocturnal marine stratocumulus, *J. Atmos. Sci.*, *62*(1), 88–106.

vanZanten, M. C., et al. (2011), Controls on precipitation and cloudiness in simulations of trade-wind cumulus as observed during RICO, *J. Adv. Model. Earth Syst.*, *3*, M06001, doi:10.1029/2011MS000056.

Vickers, D., and L. Mahrt (2010), Sea-surface roughness lengths in the midlatitude coastal zone, *Q. J. R. Meteorol. Soc.*, *136*(649), 1089–1093.

Wang, Q., and D. H. Lenschow (1995), An observational study of the role of penetrating cumulus in a marine stratocumulus-topped boundary layer, *J. Atmos. Sci.*, *52*(16), 2778–2787.

Wood, R. (2012), Stratocumulus clouds, *Mon. Weather Rev.*, *140*, 2373–2423.

Wood, R., and C. S. Bretherton (2004), Boundary layer depth, entrainment, and decoupling in the cloud-capped subtropical and tropical marine boundary layer, *J. Clim.*, *17*(18), 3576–3588.

Wyant, M. C., C. S. Bretherton, H. A. Rand, and D. E. Stevens (1997), Numerical simulations and a conceptual model of the stratocumulus to trade cumulus transition, *J. Atmos. Sci.*, *54*(1), 168–192.

Yamaguchi, T., and D. A. Randall (2012), Cooling of entrained parcels in a large-eddy simulation, *J. Atmos. Sci.*, *69*(3), 1118–1136.

Yamaguchi, T., D. A. Randall, and M. F. Khairoutdinov (2011), Cloud modeling tests of the ULTIMATE-MACHO scalar advection scheme, *Mon. Weather Rev.*, *139*(10), 3248–3264.

Zhang, M., C. Bretherton, M. Webb, and A. Siebesma (2010), CFMIP-GCSS intercomparison of large eddy models and single column models (CGILS), *GEWEX News*, *20*, 6–8.

Zhu, P., et al. (2005), Intercomparison and interpretation of single-column model simulations of a nocturnal stratocumulus-topped marine boundary layer, *Mon. Weather Rev.*, *133*(9), 2741–2758.

Corresponding author: J. J. van der Dussen, Department of Geoscience and Remote Sensing, Delft University of Technology, Stevinweg 1, Delft, NL-2628 CN, Netherlands. (j.j.vanderdussen@tudelft.nl)